Dimerization and Structure Formation of Colloids via Capillarity at Curved Fluid Interfaces

Alismari Read, Sreeja Kutti Kandy, Iris B. Liu, Ravi Radhakrishan, Kathleen J. Stebe

1 Interaction Potential with Higher Order Modes

Here we derive a more general expression for the interaction potential of two particles, A and B, separated by distance r_{AB}, interacting on a curved interface in the limit of small slope. We will derive the local description of the host interface with higher order terms and express the particle-sourced disturbance owing to the pinned, undulated contact line in terms of a multipole expansion. With these two expressions and using the method of reflections, we will find the interaction potential of two particles on a curved interface with higher order modes. The definitions for β_i, α_i, H_m, R_m, ψ, and L_i remain the same.

We first find an expression for the local shape of the host interface around the center of particle A. The interface shape in a region sufficiently close to the circular post is well approximated by:

$$h(L) = H_m - R_m \tan\psi \ln\left(\frac{L}{R_m}\right). \tag{1.1}$$

In the limit of $\lambda = \frac{a}{L_A} < 1$, we expand the above equation in a Taylor series expansion at (L_A, β_A). We perform a coordinate transformation using the following relationships between the global coordinate (X, Y) and the local particle coordinate (x_p, y_p),

$$L^2 = X^2 + Y^2 \tag{1.2}$$

$$X = L_A \cos\beta_A + x_p \tag{1.3}$$

$$Y = L_A \sin\beta_A + y_p. \tag{1.4}$$

The logarithmic part in (1.1) can be expanded as,

$$\ln\left(\frac{L}{R_m}\right) = \frac{1}{2}\ln\left(\frac{L^2}{R_m^2}\right) = \frac{1}{2}\ln(L^2) - \frac{1}{2}\ln(R_m^2). \tag{1.5}$$

By using the coordinate transformations and scaling variables with a, the first term becomes:

$$\ln(L^2) = \ln(L_A^2) + \ln(1 + 2\lambda(\tilde{x_p}\cos\beta_A + \tilde{y_p}\sin\beta_A) + \lambda^2(\tilde{x_p^2} + \tilde{y_p^2})). \tag{1.6}$$

Since λ is small we can expand the second ln term in a power series up to powers of λ^3. After some algebraic manipulation and casting variables in polar coordinates we obtain:

$$\ln(L^2) = \ln(L_A^2) + 2\lambda\tilde{r_A}\cos(\phi_A - \beta_A) - \lambda^2\tilde{r_A}^2\cos 2(\phi_A - \beta_A) + \frac{2}{3}\lambda^3\tilde{r_A}^3\cos 3(\phi_A - \beta_A). \tag{1.7}$$

Substituting the above equation in the dimensionless form of equation (1.1) and using Equation (1.5), the dimensionless interface profile is:

$$h(\tilde{r_A}, \phi_A) = \tilde{H_m} - \tilde{R_m}\tan\psi \left(\frac{1}{2}\frac{L_A^2}{R_m^2} + \lambda \tilde{r_A} \cos(\phi_A - \beta_A) - \frac{1}{2}\lambda^2 \tilde{r_A}^2 \cos 2(\phi_A - \beta_A) + \frac{1}{3}\lambda^3 \tilde{r_A}^3 \cos 3(\phi_A - \beta_A) \right). \tag{1.8}$$

The first term inside the parentheses is the change in local interface height from the neighbor. Absent body forces, the particle changes the height of its center of mass to this new reference plane. The second term is a change in slope. Absent body torques, the particle rotates tangent to this surface to eliminate such a dipolar distortion. The final terms are leading order terms and they survive. Therefore,

$$h(\tilde{r_A}, \phi_A) = \tilde{R_m}\tan\psi \left(\frac{1}{2}\lambda^2 \tilde{r_A}^2 \cos 2(\phi_A - \beta_A) - \frac{1}{3}\lambda^3 \tilde{r_A}^3 \cos 3(\phi_A - \beta_A) \right). \tag{1.9}$$

Noting that $\Delta C_o^A = \frac{2R_m \tan\psi}{L_A^2}$, the disturbance created by the host interface around the particle in dimensional form is:

$$h_{host}^A(r_A, \phi_A) = \frac{\Delta C_o^A}{4} r_A^2 \cos 2(\phi_A - \beta_A) - \frac{1}{6}\frac{\Delta C_o^A}{L_A} r^3 \cos 3(\phi_A - \beta_A). \tag{1.10}$$

A spherical particle on the fluid interface disturbs the interface height owing to its pinned undulated contact line. This particle-sourced disturbance can be expressed as,

$$h_p^A(r_A, \phi_A) = h_{2A}\frac{a^2}{r_A^2}\cos 2(\phi_A - \alpha_2 A) + h_{3A}\frac{a^3}{r_A^3}\cos 3(\phi_A - \alpha_3 A), \tag{1.11}$$

where the subscripts 2, and 3 refer to the mode of deformation, i.e. quadrupolar and hexapolar modes, and α_n is the phase angle for mode n. The solution to the shape of the interface around particle A in the absence of B on the curved interface is the sum of the following contributions:

$$h_{iso}^A(r_A, \phi_A) = h_p^A(r_A, \phi_A) + h_{host}^A(r_A, \phi_A) + h_{ind,host}^A(r_A, \phi_A), \tag{1.12}$$

where $h_{ind,host}^A(r_A, \phi_A) = -\frac{\Delta {C_o}^A a^2}{4 r_A^2}\cos 2(\phi_A - \beta_A) + \frac{1}{6}\frac{\Delta {C_o}^A a^3}{L_A r_A^3}\cos 3(\phi_A - \beta_A)$ is the distortion in the interface that enforces the contact line boundary condition. However, if A and B are near each other they change the shape of the interface in each other's vicinity. The disturbance created by B near A can be found by expanding the disturbances made by particle B around the center of A in a Taylor series. Like before we are only interested in the curvature field created by particle B near A and higher order distortions since lower order terms cannot persist. Thus the disturbance is given by:

$$\begin{aligned} h_{BatA} = 3a^2\frac{h_{2B}}{r_{AB}^4} r_A^2 \cos 2(\phi_A + \alpha_{2B}) - \frac{3\Delta C_o^B}{4}\frac{a^4}{r_{AB}^4} {r_A}^2 \cos 2(\phi_A + \beta_B) \\ - 10a^3\frac{h_{3B}}{r_{AB}^6} r_A^3 \cos 3(\phi_A + \alpha_{3B}) - \frac{5}{3}\frac{\Delta C_o^B}{L_B}\frac{a^6}{r_{AB}^6} {r_A}^3 \cos 3(\phi_A + \beta_B). \end{aligned} \tag{1.13}$$

We can now solve for the height of the interface around particle A owing to this curvature field and higher order disturbances by solving the Laplace equation subject to these two boundary conditions:

$$h^A(r_A = a, \phi_A) = h_{2A}\cos 2(\phi_A - \alpha_{2A}) + h_{3A}\cos 3(\phi_A - \alpha_{3A}) \tag{1.14}$$

$$\lim_{r_A \to \infty} h^A(r_A, \phi_A) = h^A_{host} + h_{BatA}. \tag{1.15}$$

The solution to the height is composed by summing the following heights:

$$h^A(r_A, \phi_A) = h^A_p + h^A_{host} + h_{BatA} + h^A_{ind,host} + h_{ind,BatA}, \tag{1.16}$$

where

$$h^A_{ind,host} = -\frac{\Delta C^A_o}{4}\frac{a^4}{r_A^2}\cos 2(\phi_A - \beta_A) + \frac{\Delta C^A_o}{6L_A}\frac{a^6}{r_A^3}\cos 3(\phi_A - \beta_A) \tag{1.17}$$

$$\begin{aligned} h_{ind,BatA} = &-3a^2\frac{h_{2B}}{r_{AB}^4}\frac{a^4}{{r_A}^2}\cos 2(\phi_A + \alpha_{2B}) + \frac{3\Delta C^B_o}{4}\frac{a^4}{r_{AB}^4}\frac{a^4}{{r_A}^2}\cos 2(\phi_A + \beta_B) \\ &+ 10a^3\frac{h_{3B}}{{r_{AB}}^6}\frac{a^6}{{r_A}^3}\cos 3(\phi_A + \alpha_{3B}) + \frac{5}{3}\frac{\Delta C^B_o}{L_B}\frac{a^6}{{r_{AB}}^6}\frac{a^6}{{r_A}^3}\cos 3(\phi_A + \beta_B). \end{aligned} \tag{1.18}$$

By calculating the change in free energy, ΔE, subtracting curvature indenpendent terms, and repeating the same calculations for particle B in the vicinity of A, the net interaction energy is:

$$\begin{aligned} \frac{E_{net,hex}}{\gamma\pi a^2} = &\frac{\Delta C^A_o}{2}\Big[- h_{2A}\cos(2(\beta_A - \alpha_{2A})) + \frac{a}{L_A}h_{3A}\cos(3(\beta_A - \alpha_{3A}))\Big] \\ &+ \frac{\Delta C^B_o}{2}\Big[- h_{2B}\cos(2(\beta_B - \alpha_{2B})) + \frac{a}{L_B}h_{3B}\cos(3(\beta_B - \alpha_{3B}))\Big] \\ &+ \frac{a^2}{r_{AB}^4}\Big[- 12h_{2A}h_{2B}\cos(2(\alpha_{2A} + \alpha_{2B})) + 60h_{3A}h_{3B}\frac{a^2}{r_{AB}^2}\cos(3(\alpha_{3A} + \alpha_{3B}))\Big] \\ &+ \frac{\Delta C^B_o a^4}{2r_{AB}^4}\Big[3h_{2A}\cos(2(\alpha_{2A} + \beta_B)) + 10h_{3A}\frac{a^3}{r_{AB}^2 L_B}\cos(3(\alpha_{3A} + \beta_B))\Big] \\ &+ \frac{\Delta C^A_o a^4}{2r_{AB}^4}\Big[3h_{2B}\cos(2(\alpha_{2B} + \beta_A)) + 10h_{3B}\frac{a^3}{r_{AB}^2 L_A}\cos(3(\alpha_{3B} + \beta_A))\Big]. \end{aligned} \tag{1.19}$$

2 Particle Dynamics

Here we present other set of pairs interacting on the curved interface and their respective dynamics. The L versus t plots show a comparison between theoretical predictions using Equation 12 versus observed trajectory. The pair in Figure S1 show the same behavior as the one described in the main text where both particles are migrating uphill and then at some distance particle A reverses direction to form a pair with B. However for the pairs in Fig.S2 the trajectory shows particle A reversing back to form a pair. This is due to particles with similar quadrupolar magnitudes being at close proximity at further distances from the post compare to the first case. For all cases the magnitude of the quadrupolar distortions is the sole free parameters fit in this comparison.

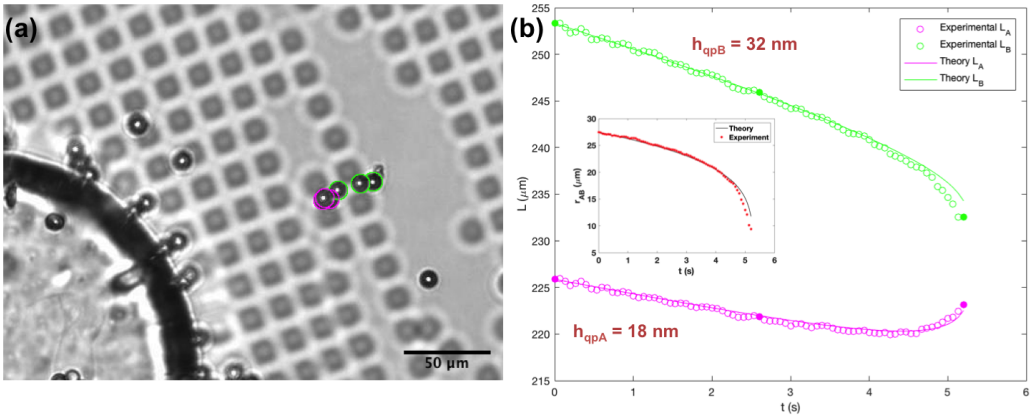

Figure S1: **Pair** #1 (a) Time stamped image of two particles migrating toward the post and forming a dimer ($t = 0s, t = 2.6s, t = 5.20s$) on the curved interface with $\psi = 14^o$. (b) The trajectory of each particle in this dimer (symbols) in terms of position with respect to the micropost L versus time t. Theory with best fit amplitudes for quadrupolar distortions (solid lines). *Inset*: inter-particle distance r_{AB} versus time t.

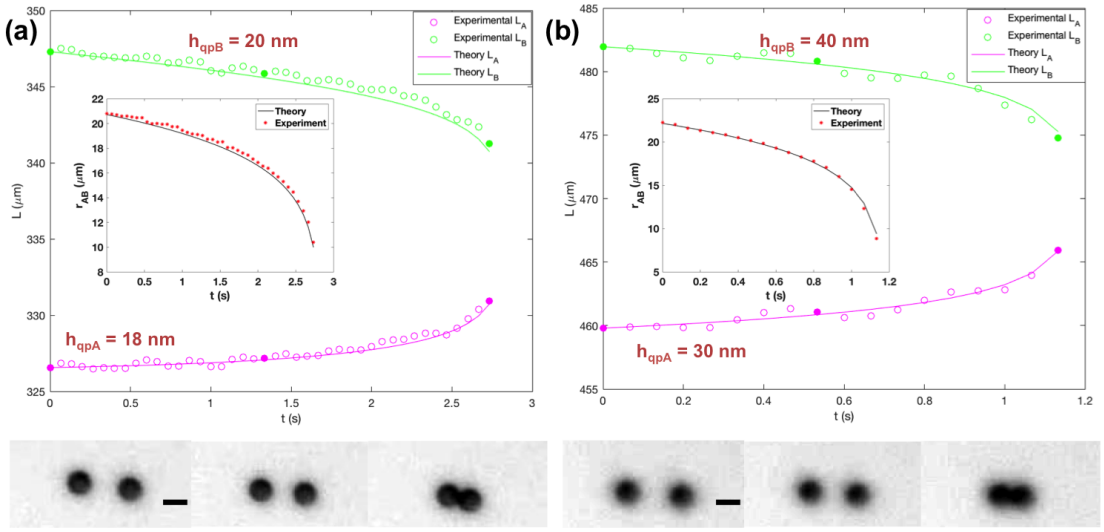

Figure S2: The trajectory (symbols) of each particle in the dimer shown underneath in terms of position with respect to the micropost L versus time t on the curved interface with $\psi = 12^o$. Theory with best fit amplitudes for quadrupolar distortions (solid lines). *Inset*: inter-particle distance r_{AB} versus time t. (a) **Pair** #2 ($t = 0s, t = 1.33s, t = 2.73s$). (b) **Pair** #3 ($t = 0s, t = 0.53s, t = 1.13s$). Scale bar = 10 μm

The following videos show 10 μm polystyrene particles interacting on the water-hexadecane curved interface and forming a pair.

Video S1: Trajectory is shown in Fig.2(c-d). 1.5X Real Time. $\psi = 12^o$

Video S2: Trajectory is shown in Fig.S1. 1.5X Real Time. $\psi = 14^o$

Video S3: Trajectory is shown in Fig.S2(a). 1.5X Real Time. $\psi = 12^o$

Video S4: Trajectory is shown in Fig.S2(b). 1.5X Real Time. $\psi = 12^o$

3 Isolated Particle on Curved Interface

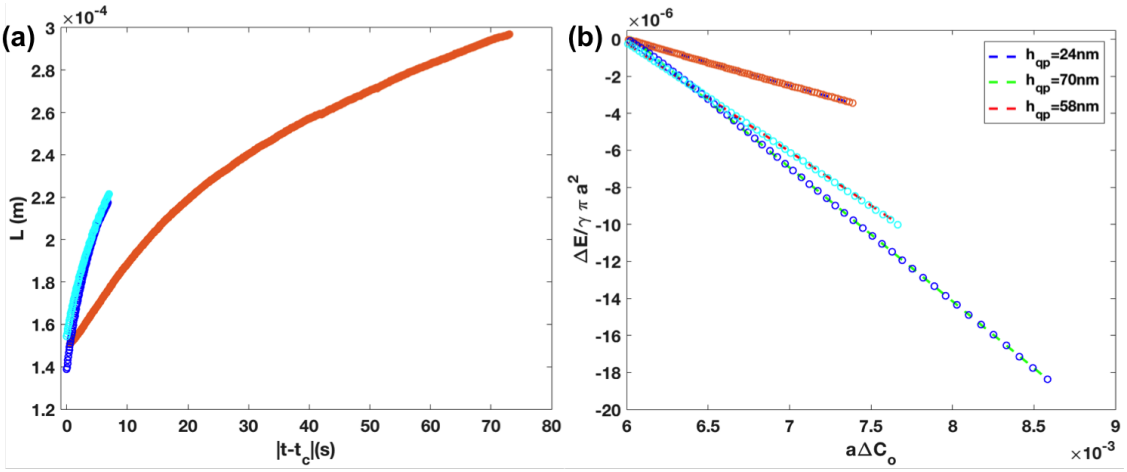

Figure S3: (a) Trajectory of spheres around the cylindrical micropost - radial distance of the migrating microsphere from the center of the post as function of time remaining until contact with the post. (b) Comparison of predicted curvature capillary energy (solid line) against the extracted energy from experiment for the trajectories (open circles).

The migration of polystyrene colloidal spheres with mean diameter of $2a = 10\ \mu m$ and root mean squared roughness of 15–40 nm on interfaces with slope 15–18^o has been previously studied. Here we study some isolated particles to show again how their behavior differs from pairs on the curved interface. Particle trajectories (Fig.S3(a)) showed that spheres are propelled faster in the region closer to the post where the magnitude of the deviatoric curvature was greater consistent with previous observations. Particles also move along a radial path as expected since the capillary energy for the interaction between the particles and the curvature field has no dependency on the azimuthal angle ϕ, $E^A_{iso} = \gamma\pi a^2 \frac{h_{qpA}\Delta {C_o}^A}{2}$. Quantitatively we can show that the energy dissipated along the particle trajectory agrees with that expected from theory. In the limit of zero inertia the curvature capillary energy used to move particles is balanced by viscous dissipation. The total energy can be extracted from the trajectories by integrating the drag force as, $\Delta E = \int_{L_i}^{L_f} F_{drag} dL$, where L_i is the reference point and L_f is an arbitrary point along the trajectory. Plotting the energy dissipated normalized by $\gamma\pi a^2$ against $a\Delta C_o$ shows that the relationship is linear as can be seen in Fig.S3(b). The magnitude of the quadrupolar mode h_{qp} inferred from these trajectories are consistent with values previously reported (between $20 - 130nm$).

Video S5: 10 μm polystyrene particle migrating on the water-hexadecane curved interface. Respective trajectory is shown in orange in Fig.S3(a). 1.5X Real Time. $\psi = 12^o$

Video S6: 10 μm polystyrene particle migrating on the water-hexadecane curved interface. Respective trajectory is shown in blue in Fig.S3(a). 1.5X Real Time. $\psi = 12^o$

Video S7: 10 μm polystyrene particle migrating on the water-hexadecane curved interface. Respective trajectory is shown in cyan in Fig.S3(a). 1.5X Real Time. $\psi = 13^o$

4 Exploring Pair Assembly through Force and Torque Calculations

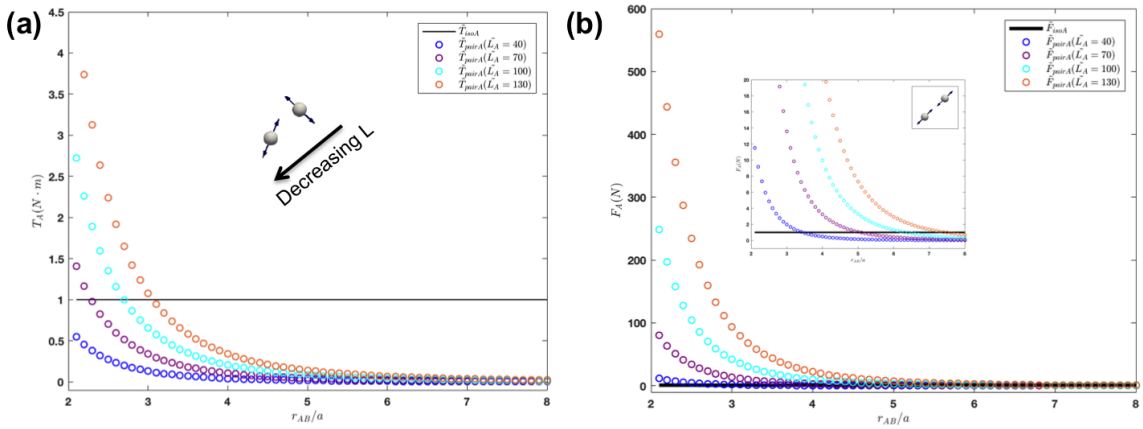

Figure S4: (a) Capillary torque and (b) capillary force of particle A as a function of dimensionless inter-particle distance, for a typical system with $\psi = 15^o$, $a = 5\ \mu m$, $R_m = 125\ \mu m$, and $h_{qpA} = h_{qpB} = 30\ nm$. Straight line corresponds to the capillary torque/force due to particle-curvature interactions. Curves with open circles correspond to the capillary torque/force due to particle-particle interactions at different distances from the post ($\tilde{L_A} = \frac{L_A}{a}$).

The net capillary energy for particle i in the vicinity of particle j is given by:

$$\frac{E^i_{net}}{\gamma\pi a^2} = -\frac{h_{qpi}\Delta C^i_o}{2}\cos(2(\beta_i - \alpha_i)) - \frac{6h_{qpi}h_{qpj}a^2}{r^4_{ij}}\cos(2(\alpha_i + \alpha_j)) + \frac{3h_{qpi}\Delta C^j_o a^4}{2r^4_{ij}}\cos(2(\alpha_i + \beta_j)). \quad (4.1)$$

Substituting for ${\Delta C_o}^i$ and factoring out the isolated particle curvature migration term:

$$\frac{E^i_{net}}{\gamma\pi a^2} = -R_m \tan\psi \frac{h_{qpi}}{L^2_i}\cos(2(\beta_i - \alpha_i))\left[1 + \left\{\frac{6h_{qpj}}{R_m \tan\psi}\frac{L^2_i a^2}{r^4_{ij}}\frac{\cos(2(\alpha_i + \alpha_j))}{\cos(2(\beta_i - \alpha_i))} - \frac{L^2_i}{L^2_j}\frac{3a^4}{r^4_{ij}}\frac{\cos(2(\alpha_i + \beta_j))}{\cos(2(\beta_i - \alpha_i))}\right\}\right]. \quad (4.2)$$

For typical system parameters specified in the caption to Figure S4, we can compare the relative magnitudes of the terms in curly brackets in Equation 4.2, i.e. for particle A, to determine at what inter-particle distance the pair interaction wins over the isolated curvature interaction. For simplicity we will do this for an idealize case in which particles are behind one another, $r_{AB} = L_B - L_A$, initially with a random orientation of the quadrupolar axes (inset in Figure S4). Let particle A be initially at a distance from the post anywhere between $L_A = 200$–$500\ \mu m$, which is the region studied in experiment. Calculations show that r_{AB} must be approximately 10–13 μm for the terms in curly bracket to be comparable to one. This suggest that these terms are near field and particles will dimerize once they are near each other depending on their position from the post. Energy gradients as particles rotate at a fixed position on the interface generate capillary torques. The curvature-related forces decay faster with distance from the micropost than do the curvature-related torques. This shows to be key in determining particle alignment with respect to the curvature and nearby particles even before migration occurs. The capillary torque for the capillary energy of A in the vicinity of B, is equal to $T_{capA} = \frac{\partial E_A}{\partial \alpha_A}$. We can calculate the torque experienced by A to rotate its quadrupolar axes from the initial orientation. By splitting the torque in two parts, T_{isoA} and T_{pairA}, and normalizing by T_{isoA}, we compare their relative magnitudes. Fig.S4(a) shows this comparison at different distances from the post as

we decrease the distance between A and B. Clearly the closer the particles are to the post the most near contact they have to be to form mirror symmetric dimers without influence from the underlying curvature, i.e. $T_{pairA} > T_{isoA}$. Otherwise T_{isoA} wins and particles align with the curvature field. Energy gradients with position generate capillary forces, F_{cap}, that bring particles together, F_{pairA}, or propel them to regions of high curvature gradients, F_{isoA}, once they align. Fig.S4(b) shows a comparison at different distances from the post between these two forces normalized by, F_{isoA}, as the distance between A and B is decreased. It is evident from this comparison that at a specific L location the closer the particles are the stronger the force to pair formation. Thus as particles approach one another pair interaction starts becoming more and more important, $F_{pairA} > F_{isoA}$, leading to the formation of dimers on the curved interface.

This analysis show that pair assembly is complex as the terms that dominate dimerization depend on many parameters. Generally pairs of particles once adsorbed first experience a torque that either aligned them with each other or the curvature field. Once align they migrate to sites of high curvature gradients or form dimers.

5 Calculating Fractal Dimension

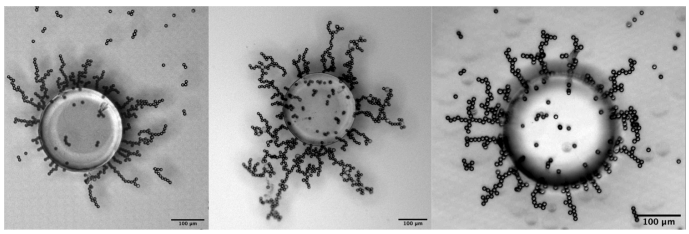

Figure S5: Fractals formed around the cylindrical micropost on the curved fluid interface. Particles on top of the micropost are not in the fluid interface and are not considered as part of the structure.

In Fig.1(d) we present a fractal structure formed around the cylindrical micropost by a dense suspension of polystyrene spheres interacting via capillary interactions. Other fractals formed around the cylindrical micropost are shown in Fig.S5. These structures have fractal dimension ranging from 1.4–1.6. Here we describe how we calculated fractal dimension for these fractals and how we compared this to simulated DLA fractals.

The fractal structures were characterized by calculating their respective Hausdorff Dimension (popularly fractal dimension). The Hausdorff dimension is an integer for sets of points that define smooth shapes in traditional geometry, which agree with dimension in Euclidian space [1]. For other less simple objects like fractals, based only on scaling properties, the Hausdorff dimension is a fraction. Fractal dimension is defined in the following way:

$$D = \frac{\log N}{\log(1/s)} \rightarrow N = s^{-D}, \tag{5.1}$$

where N is the total number of segments needed to cover a perimeter of length L where each N segment has length s. The fractal dimension of the structures were specifically calculated using the "box counting" method. In this technique boxes of different sizes are used to cover the 2D image of the fractal formed on the interface. Information on the number of boxes needed to cover the image helps in constructing a log-log plot from which the fractal dimension is obtained from the slope. There are many packages and software that have built in algorithms for box counting including ImageJ, thus we have chosen to do our analysis with the FRACLAC plugin. The boxes had length 5–315 pixels. Fig.S6(a) shows an example of this method and the resulting fractal dimension for the fractal in Fig.1(d), $D = 1.52$.

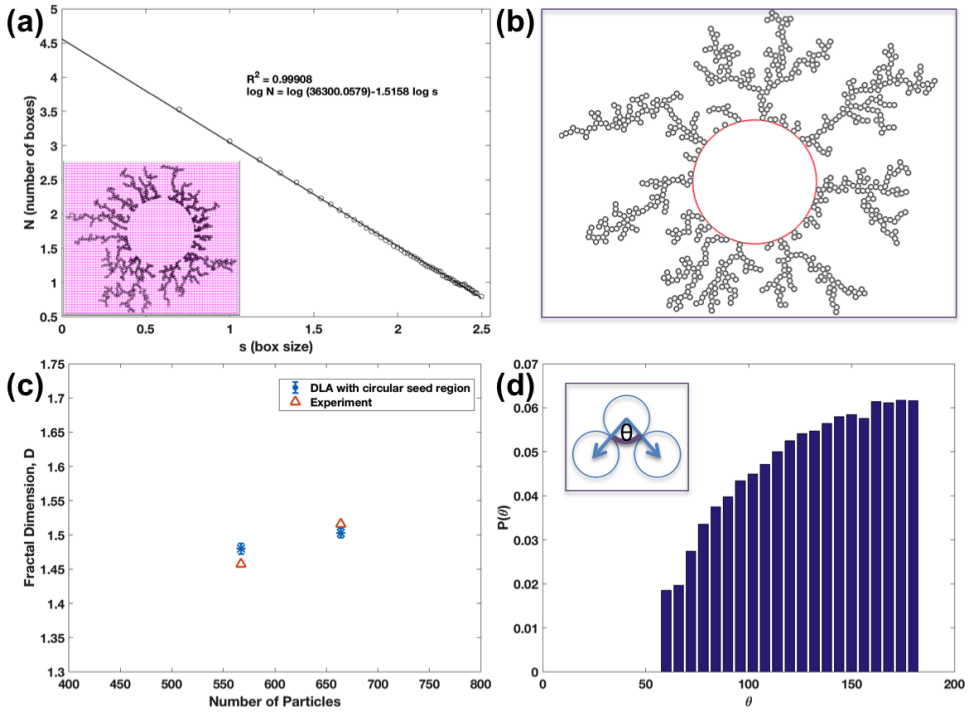

Figure S6: **Fractal dimension analysis** (a) Log-log plot of box number vs box size showing the fractal dimension for fractal in Fig.1(e). *Inset:* schematic showing boxes covering the 2D fractal image. (b) Simulated DLA fractal with circular seed region and 664 particles. (c) Fractal dimension D versus number of particles N for fractals obtained through experiment and DLA simulations. (d) Angle distribution between particle centers for simulated fractal in (b). *Inset:* schematic showing angle between particle centers used for angle distribution calculations.

The fractal dimension obtained from the analysis of the different capillary fractals, $D = 1.4$–1.6, is lower than that of the reference fractal dimension of 1.71 for a diffusive limited aggregation (DLA) structure. To understand what influence curvature had on the topology of the fractal and its dimension, a DLA fractal with a circular seed region (i.e. the post) was simulated (Fig.S6(b)). This was done by initializing the circular seed at the origin and then releasing particles one at a time at some radius larger than the cluster radius, allowing them to randomly walk until they touch and attached to an aggregate. If particles crossed a killing radius much larger than the system size, they would be annihilated. This process was continued until all the particles were attached or killed. Fig.S6(c) shows how the fractal dimension compares for different number of particles. Results show that for a fractal with a seed region resembling the post and the same number of particles as in experiments, the fractal dimension was closely the same. These results shows that curvature does not have an influence on the topology of the fractal, however as explained in the main text, the angle distribution between particle centers yields evidence of different mechanisms behind the formation of these structures. Fig.S6(d) shows that important peaks demonstrating the importance of particle-particle and particle-curvature interactions on the curved interface are absent in the DLA structure.

To explain why the fractal dimension was lower than 1.71 a larger fractal with $\sim$ 6000 particles was simulated (Fig.S7(a)). The fractal dimension for this fractal came out to be $\sim$ 1.66, which is close to 1.71. We suspected that the value was lower due to the seed being larger than the particles leading to larger branch gaps. To confirm this, another fractal formed around a particle size seed was simulated (Fig.S7(b)). In fact the fractal dimension for this fractal was 1.7180, pretty close to the established value. Therefore, we were able to conclude that the lower value was due to discrete finite size effects for the smaller fractals.

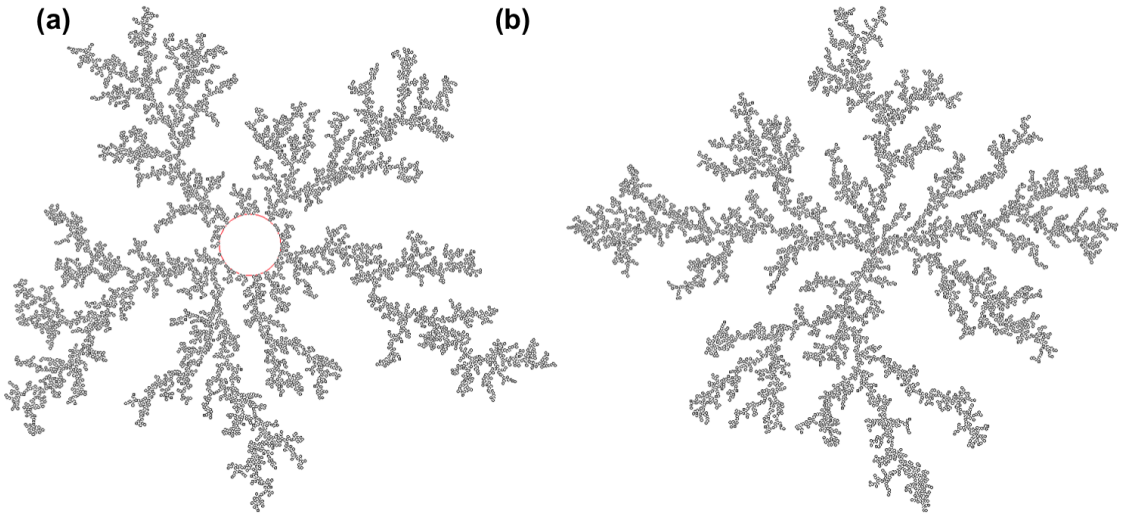

Figure S7: **Simulated DLA fractals** (a) Fractal formed around a seed region resembling the post, $D = 1.6580$. (b) Fractal formed around a particle size seed, $D = 1.7180$.

6 Structure Formation

When comparing the angle distribution in the clusters between experiments and MC simulations, we observe very clear peaks in the simulations for 60^o, 90^o, and 180^o, which are kind of blurred in the experiments. In the main text we explained that likely sources of discrepancy between the observed and simulated angle distributions are the inclusion of only the two leading order modes in the contact line undulation, and the assumption of fixed amplitudes of these two modes on all particles. In simulations, the particle translation is not restricted to a grid and can access all positional degrees of freedom for the interface. The value of translational displacement ϵ is chosen from a uniform random number distribution such that $-0.05\mu m \leq \epsilon \leq 0.05\mu m$ which is much smaller than the particle size of $5\mu m$. Similarly, for the rotational displacement the angular displacements are chosen such that $-\pi/200 \leq \epsilon \leq \pi/200$. Hence we do not think the translational or rotational step size would restrict the particle from exploring the configurational space.

Video S8: 10 μm polystyrene particle forming clusters on the water-hexadecane curved interface. 1.5X Real Time. $\psi = 15^o$

Video S9: Example of a cluster reorganizing. Particle within an L shape changes position in the cluster. 0.1X Real Time. $\psi = 15^o$

Video S10: Monte Carlo simulation of 10 μm particles forming clusters around the cylindrical micropost. $\psi = 15^o$

References

[1] B. B. Mandelbrot, *The fractal geometry of nature*, vol. 1. WH freeman New York, 1982.